A comprehensive diagnostic of liquid sheet targets for laser ion acceleration

Ziyang Peng[1], Zhengxuan Cao[1], Xuan Liu[1], Yinren Shou[4], Jiarui Zhao[1], Shiyou Chen[1], Ying Gao[1], Pengjie Wang[5], Zhusong Mei[1], Zhuo Pan[1], Defeng Kong[1], Shirui Xu[1], Zhipeng Liu[1], Yulan Liang[1], Tianqi Xu[1], Tan Song[1], Xun Chen[1], Qingfan Wu[1], Yujia Zhang[1], Zihao Zhang[1], Xueqin Yan[1,2,3], Wenjun Ma[1,2,3*]

1 State Key Laboratory of Nuclear Physics and Technology, Key Laboratory of HEDP of the Ministry of Education, CAPT, Peking University, Beijing, China

2 Beijing Laser Acceleration Innovation Center, Beijing, China

3 Institute of Guangdong Laser Plasma Technology, Guangzhou, China

4 Center for Relativistic Laser Science, Institute for Basic Science, Gwangju, Republic of Korea

5 Institute of Radiation Physics, Helmholtz-Zentrum DresdenRossendorf, Dresden, Germany

Email: pengjiang_123@stu.pku.edu.cn

Corresponding author: wenjun.ma@pku.edu.cn

Abstract

To meet the demands of laser ion acceleration at a high repetition rate, we have developed a comprehensive diagnostic system for real-time and in-situ monitoring of liquid sheet targets (LST) generated by the collision of two liquid jets. The spatially resolved rapid characterizations of a LST's thickness, flatness, tilt angle and position are fulfilled by different subsystems with high accuracy. With the help of the diagnostic system, we reveal the dependence of thickness distribution on collision parameters and the determinants of LSTs' flatness and tilt angle, which are essential for applications of laser-driven ion acceleration and others.

Keywords: liquid sheet targets; diagnostic; laser ion acceleration

Introduction

The interaction of ultra-intense laser pulses with micrometer-thin film targets can accelerate ions to very high energy within a few micrometers. Near-100-MeV protons and 1.2-GeV Au ions have been generated by laser acceleration[1][2]. This

10.1017/hpl.2023.101

novel ion acceleration method attracts widespread attention as it can produce ultrashort ion pulses in a short distance, which is highly appealing for applications such as proton imaging, pulsed neutron generation, and FLASH radiotherapy[3][4]. Many of them require a high average flux, which should be achieved by shooting targets at a high repetition rate. However, solid films, the most widely used targets in previous studies, are not suitable for long-term high repetition rate shooting. After each laser-target interaction, the film in an area of about a few mm2 around the focal spots would be completely destroyed. If they are shot at kHz, for example, supplying the targets in the vacuum would be a big challenge, not to mention the cost and debris damage to the optical components in the target chamber.

Superior to solid films, free-flowing micrometer-thin liquid sheets are promising targets for high-repetition-rate laser ion acceleration[5]. They are made of continuous liquid flow without any supporting substrate. Under the irradiation of an ultra-intense laser pulse , the damaged area can be repaired spontaneously in 0.1 ms, enabling continuous shooting at a repetition rate up to kilohertz or higher[5]. Therefore, liquid sheet targets (LST) draw increasing interest in the field of laser ion acceleration.

While still in its early stages, some pioneering work had successfully employed LST in experiments. In 2018, Morrison et al. first achieved the generation of 2.3 MeV protons from LST at kHz repetition rate for the first time[6], and a few years later Valdes et al. obtained 3.5-MeV protons from LST at a higher vacuum degree[7]. Deuterons with energies up to 4.4 MeV were also generated by using LST made of heavy water[8]. Nevertheless, these works lack a complete characterization of LSTs. It has been known that the film's position with respect to the focal spot and its thickness significantly influences the energy of ions. The tilt angle and flatness of the film would affect the direction and divergence of the ion beam. Therefore, for optimized and stable ion acceleration, comprehensive characterization of films is very necessary.

In this work, we present an online diagnostic system for the comprehensive characterization of liquid sheets used in laser-driven ion acceleration. First, an overview of our LST generation and characterization system is presented. Afterwards, the components of the system for the measurement of LST's thickness, flatness, tilt angle and spatial position are described separately in 4 sections. Analysis methods are also given. At last, a summary and future prospects will be provided in the final section.

https://doi.org/10.1017/hpl.2023.101 Published online by Cambridge University Press

LST Generation and Characterization System

The liquid sheet was generated with our homemade colliding-jets device, and relevant information can be found in our previous publication[9]. Fig.1(a) shows the formation process of a liquid sheet: two liquid jets eject from a capillary tube with a diameter of 50 μm and collide at a speed of approximately 20 m/s, forming a collision angle of 60° (2θ). After the collision, the lateral momentum of the two jets cancels out each other and forms a closed liquid sheet in the orthogonal direction due to the effect of surface tension, as shown in Fig.1(b). In this work, we have made improvements to the device, with a total of eight degrees of freedom to regulate the sheets, including six dimensional translation and rotation, and the relative two-dimensional adjustment between the two jets. These degrees of freedom are conducive to stable control and precise characterization of liquid sheets. The liquids were driven by two high-performance liquid chromatography (HPLC) pumps (Shimadzu, LC-20ADXR) and injected into two capillary tubes respectively. The back pressure is usually several tens MPa, depending on the flow rate, capillary length, and viscosity of the liquid. In this article, the data are obtained by default using a glycerol aqueous solution with a mass fraction of 50%. Glycerol aqueous solutions with a mass fraction between 30% and 70% can operate stably in our system, but the sheet properties may vary. This type of liquid is cheap, non-toxic, and has a low saturated vapor pressure, making it ideal for LSTs.

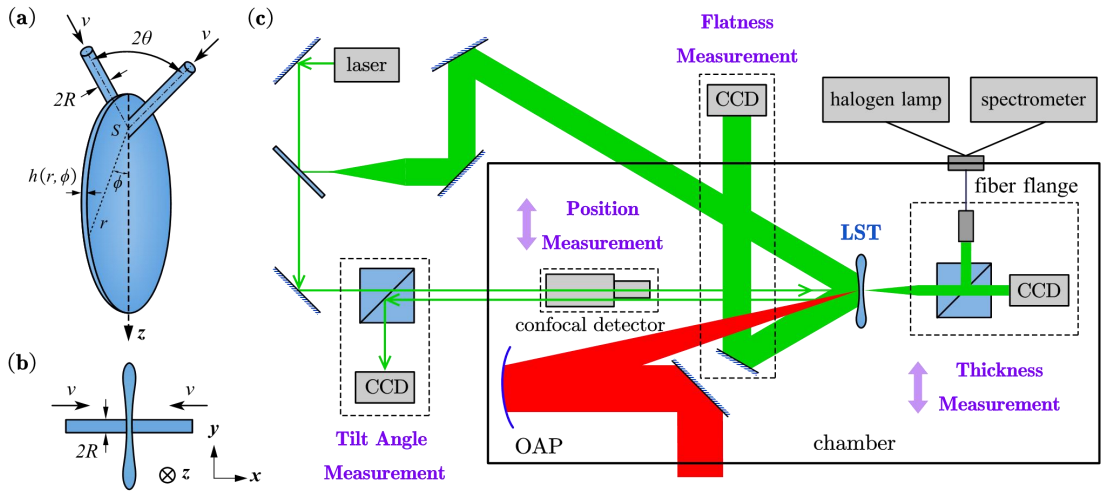

Fig.1 (a)Schematic of the liquid sheet generation, (b)Top view of the liquid sheet generation, (c)Overview of the main modules of the diagnostic system.

Fig.1(c) is an overview of the diagnostic system, which allows for real-time and spatially resolved characterization of LST's thickness, flatness, tilt angle and position fulfilled by different subsystems. The dashed boxes represent these subsystems, and

https://doi.org/10.1017/hpl.2023.101 Published online by Cambridge University Press

the purple words next to them describe their functions. The solid box represents the vacuum chamber, with LST located near the center of the chamber in fig.1(c). The red laser represents the main laser, which is focused on LST by an OAP. The green light on the left side of LST represents a monochromatic probe light, while the green light on the right side represents a broad-spectrum probe light.

It should be noted that fig.1(c) is not drawn to scale. On the left side of LST, only the confocal detector is very close to the sheet (about 20 mm), and it cannot work simultaneously with tilt angle measurement. Typically, the confocal detector is moved away by a motor after the position measurement, so there are actually no obstacles on the optical path of the main laser, and the system can operate for small f-number OAP (f/1.5, for example). Further details of the subsystems will be presented in the following sections sequentially.

Thickness Measurement

The thickness of the targets significantly affects ion energy and even the acceleration mechanism[10]. Therefore, it's essential to measure the thickness of the liquid sheet accurately. This could be challenging because LSTs are self-supporting and unable to withstand external force, making contact measurements inapplicable. Besides, the thick edge of the sheet also hinders thickness measurement using side imaging[11]. To address these challenges, we measure the thickness of a LST using the reflected white light spectrum from the film surface. In the following text, we will refer to this method as reflectance spectroscopy.

The schematic diagram of our device can be found in the upper right corner of fig.1(c). The halogen lamp and spectrometer are both placed outside the chamber, and two optical fibers are bunched on the feeding flange and connected to the chamber. Fig.2(a) is a more detailed diagram: the white light emitted from a halogen lamp is focused by the microscope lens and then irradiated on LST, and the reflected light is sent back to the spectrometer via optical fibers behind the lens. The microscopic lens enables simultaneous imaging of LST, while white light provides illumination. In order to increase the signal, six optical fibers are used to collect reflected light, they hexagonally surround the central fiber that connects to the halogen lamp. Fig.2(b) shows the side and front view of LST, where the bright dot in the center of the sheet is the incident white light. The light source is connected to the six fibers here to clearly display the structure of the fiber bundles. Ordinarily, the

https://doi.org/10.1017/hpl.2023.101 Published online by Cambridge University Press

central fiber functions as the light source, while the six outer fibers gather reflected light signals, as depicted by the six blue dots in fig.2(a). The diameter of each fiber is 200 μm, and the spot focused on the sheet is approximately 20 μm. In the next section, it will be seen that the thickness of the liquid sheet can be considered uniform in such a small area.

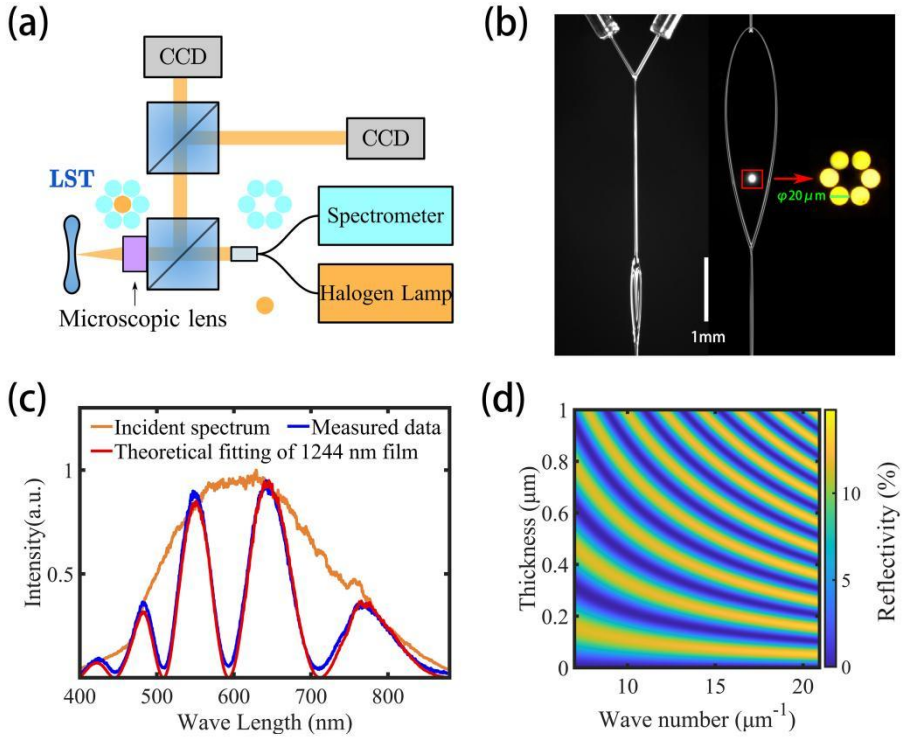

Fig.2 (a)Schematic diagram of reflectance spectroscopy, (b)Side view and front view of LST, the light source is connected to the six cores here to clearly display the measurement point, (c)A typical reflection spectrum of LST with the theoretical fitting curve, (d)Theoretical reflectivity of films with different thicknesses at different wave numbers.

Interference between the two surfaces of the film results in a chirped oscillation in the reflected light spectrum (it displays gradually changing periods, with higher frequency at short wavelengths and lower frequency at long wavelengths). The reflectivity follows equation (1), where $\delta(h,\lambda,\theta)=\frac{4\pi n(\lambda)h\cos\theta'}{\lambda}$ is the phase difference, λ is the wavelength of light, θ is the angle of incidence and θ' is the refraction angle in film, $R_0(\lambda,\theta)$ is the interface reflectivity determined by Fresnel law, h is the thickness of film and $n(\lambda)$ is the refractive index of the material[12]:

$$R(h,\lambda,\theta)=\frac{4R_0(\lambda,\theta)\sin^2[\delta(h,\lambda,\theta)/2]}{[1-R_0(\lambda,\theta)]^2+4R_0(\lambda,\theta)\sin^2[\delta(h,\lambda,\theta)/2]} \quad (1)$$

The blue curve in fig.2(c) shows a typical measured spectra from a LST, which can be well fitted by assuming a thickness of 1244 nm. However, the fitting method is

https://doi.org/10.1017/hpl.2023.101 Published online by Cambridge University Press

time-consuming and therefore difficult to use in real-time thickness measurement. Reflectance spectroscopy reported before mostly used peak positions to calculate the thickness[13], which was highly efficient, but this resulted in low information utilization and lack of accuracy.

Therefore, we develop a fast algorithm for accurately extracting thickness information from reflection spectra, and the principle is as follows: Fig.2(d) gives theoretical reflectivity values at $\theta = 0$ as functions of thickness and wave number. One can see that for films with thicknesses ranging from hundreds of nanometers to several micrometers, there are multiple peaks in the spectral range of 300-1000 nm for each thickness, and the oscillation interval in the wave number space is constant and proportional to the thickness. This can be proven by equation (1), the reflectivity exhibits a periodic oscillation, with an instantaneous frequency of $\nu(\lambda, h) = \frac{2n(\lambda)h}{\lambda^2}$, and in k-space, it is $\nu(k, h) = \frac{n(k)h}{\pi}$. This can be considered a constant if the film is uniform and the dispersion curve is known. By performing Fourier transform on the reflection spectrum and its peak directly corresponds to the thickness.

In fig.3(a) we show an example of the Fourier transform of the measured spectrum in wave number space. There are two peaks in the frequency domain, the low-frequency envelope and the high-frequency oscillation of the spectrum, respectively. The high-frequency peak position is proportional to the thickness, while the low-frequency peak is caused by the slowly changing envelope of the spectrum, as shown in the incident spectrum in fig.2(c). It should be clarified that the incident spectrum can only be used as a relative reference. We can normalize the measured spectrum by the incident spectrum to minimize the impact of the low-frequency envelope, but this does not ensure getting absolute reflectivity. It is precisely because of this that calculating the film thickness through the peak positions of the reflection spectrum is inaccurate, as the peak positions are modulated by the spectrum envelope. The inherent low-frequency component sets a lower limit for the measurement (when the oscillation frequency is close to the envelope frequency, the oscillation will be masked by the envelope). In our system, the minimum measurable thickness is about 200 nm, which is competent for the current LST (the reported thinnest liquid sheet produced by colliding-jets is 450 nm). The accuracy of this method can reach ±5 nm, and in most cases the error does not exceed 2 nm.

Based on this method, we measured the thickness of LST at different flow rates and positions. As defined in fig.1(a), we will use these symbols in the following text: h means the thickness of LST, r is the distance to the colliding point, and ϕ is the azimuth angle of the colliding point. In fig.3(b), five spectra measured at different

https://doi.org/10.1017/hpl.2023.101 Published online by Cambridge University Press

positions on LST (all five measured points here are $\phi = 0$, r takes different values) were transformed into frequency domain. The abscissa was linearly converted to thickness, and we call it the thickness spectrum. Note that the intensity of the thickness spectrum does not have a special effect, only the peak position is helpful. As the distance from the collision point increases, the liquid sheet gradually becomes thinner, and the broadening of its thickness spectrum is mainly caused by limited measurement bandwidth and dispersion, while at a distance closer to the collision point, it is mainly due to the superposition of multiple thicknesses within the measurement point (with a large thickness gradient, as will be seen in the next section).

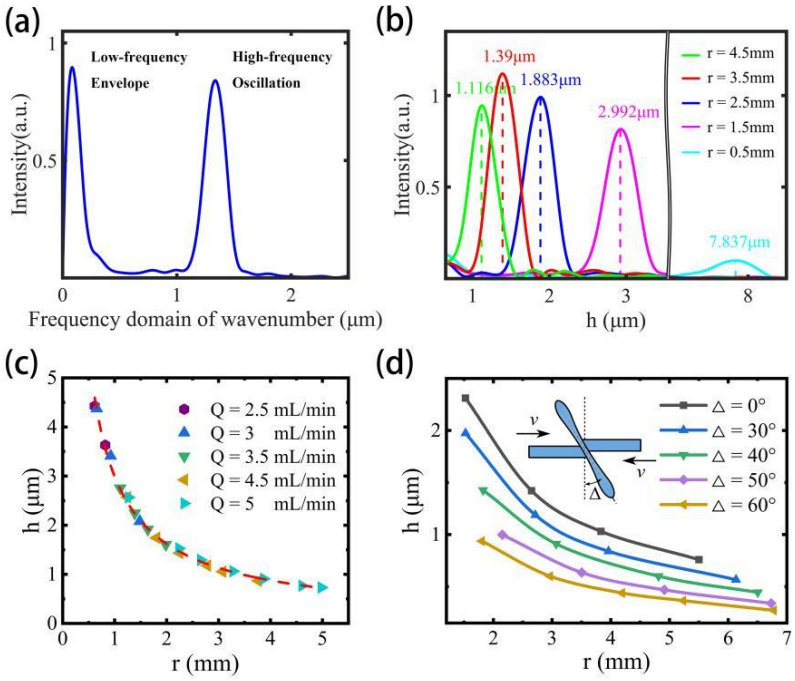

Fig.3 (a)Fourier transform of a measured spectrum in wave number space, (b)Thickness spectrum at different positions on LST, (c)Thickness of LST at different flow rates and positions, (d)Thickness of LST under different misalignment of colliding.

The overall results are shown in fig.3(c), the thickness under different flow rates seems to fall on the same curve, which means that the thickness at the same position is almost not affected by the flow rate (not exact. The measurement at fixed points indicate that the flow rate will have a slight impact on the thickness). For our application, we always hope to increase the flow rate as much as possible to generate a thinner sheet, but this is limited by factors such as system pressure and fluid instability, and usually cannot exceed 6 mL/min. Another way to obtain a thinner liquid sheet is colliding the two jets with a misalignment[14][15], as shown in the diagram in fig.4(d). Different misalignment leads to different deflection angle Δ,

https://doi.org/10.1017/hpl.2023.101 Published online by Cambridge University Press

and as the angle increases, the sheet also becomes thinner. We generated a liquid sheet about 240 nm at $\Delta = 60°$, and this is the thinnest liquid sheet formed by two colliding jets to date.

In summary, we developed an algorithm and device for online measurement of LSTs' thickness and it's combined with imaging system in a very compact way. Accuracy for most LSTs is typically within ±2 nm, and for LSTs around 250 nm, the error is ±5 nm. Additionally, we have a practical method for measuring films below 200 nm, and its details will be described in the "Tilt angle measurement" section.

Flatness Measurement

Reflectance spectroscopy measures the thickness at a specific point, and overall knowledge of the thickness distribution and flatness of a LST is also important. It helps us monitor the quality of the as-produced LST and choose the optimal shooting position. In our diagnostic system, an expanded monochromatic laser (indicated by the thick green path in fig.1(c)) is obliquely illuminating the liquid sheet, and a CCD is set in the reflection direction to image the interference fringes of the sheet, which can be used to obtain the contour information of the LST's thickness [16]-[21].

Fig.4(a) shows a typical pattern of interference fringes. In work[16][18], the local one-dimensional thickness variation is analyzed from the interference fringes, but the two-dimensional thickness distribution has not yet been obtained. Theoretically, the sine value of the phase can be derived from interference fringes, but it is not feasible to extract the thickness distribution due to blurriness in the phase. However, after analysis, we have confirmed that reconstructing the thickness distribution is still possible for liquid sheets. Here we present the first recovered two-dimensional thickness distribution of the liquid sheet. First, we assume that the intensity distribution of the expanded beam on such a small sheet is uniform, so the brightness of the interference fringes is solely related to the reflectivity of the LST. For fixed wavelength and incident angle, the wrapped phase is a single-valued function of thickness. Thus, we can uniquely obtain $\sin\delta$ according to equation(1). δ is hidden in $\sin\delta$, so the obtained phase is wrapped in the range of 0 to π, as shown in fig.4(b). Since the thickness along the axis of the liquid sheet (as shown in fig.3(c)(d)) continuously decreases from top to bottom, so the thickness at every interference fringe is $\lambda / 2n$ thicker than that at the adjacent fringe below. Based on the prior information, δ can be unwrapped using some classic algorithms[22][23]. Fig.4(c) depicts the retrieved 2D thickness distribution of the LST, where the absolute thickness value is determined through the reflectance spectroscopy measurement at

https://doi.org/10.1017/hpl.2023.101 Published online by Cambridge University Press

a single point.

It can be seen that the thickness in the upper part changes significantly compared to the relatively flat lower part, where the variation is less than 1 nm within a few micrometers. The spot of main laser in laser ion acceleration is usually several micrometers, which means the change in LST's thickness within the laser focal spot is less than 1%. This property makes the lower part more suitable for laser ion acceleration, as it provides a flat surface with a very thin thickness. Research has shown that thin films with a thick middle and thin sides may be more suitable for ultra-intense laser ion acceleration[24], while LSTs have similar properties and can be selected at locations with different thickness gradients as needed.

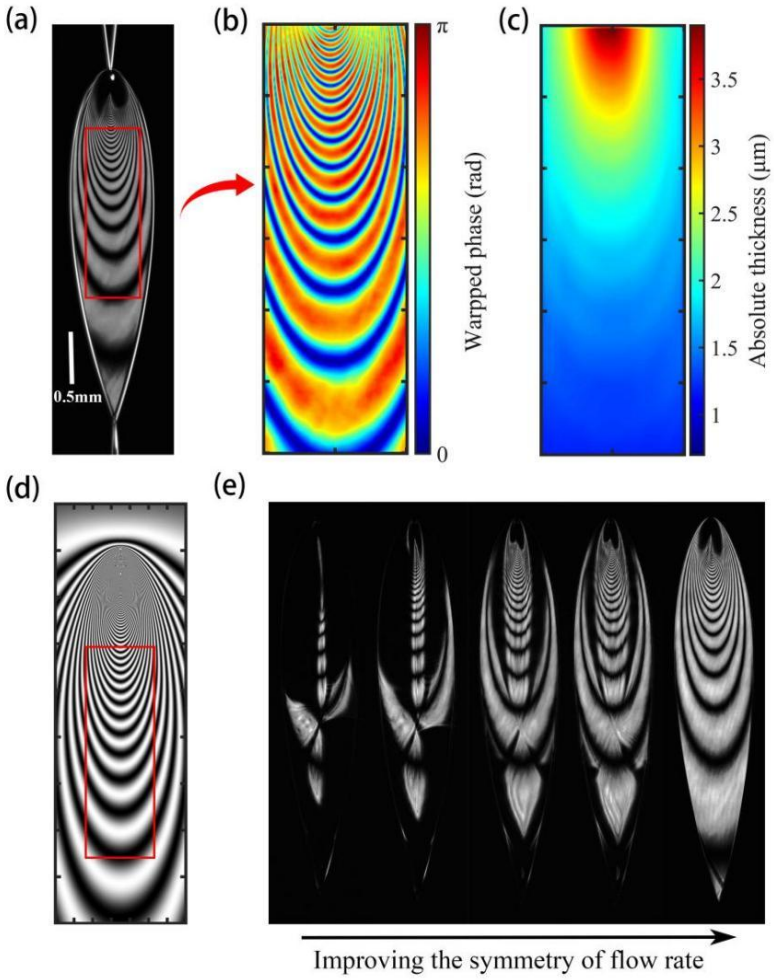

Fig.4 (a)Typical interference fringes of LST, (b) Wrapped phase in the red box of (a), (c)Thickness distribution (μm) unwrapped from (b), (d)Interference fringes corresponding to the thickness distribution of the Hasson's model, (e)The change of interference fringes with the improvement of flow symmetry.

Interference fringes are not visible near the collision point in fig.4(a), and we used Hasson's model[25] to calculate interference fringes, as shown in fig.4(d). The

https://doi.org/10.1017/hpl.2023.101 Published online by Cambridge University Press

thickness distribution given by the Hasson's model is as follows:

$$h = \frac{R^2 \sin^3 \theta}{r\left(1 - \cos\phi \cos\theta\right)^2} \tag{2}$$

From the equation and fig.4(d), it can be seen that the theoretical interference fringes closely align with the measured fringes, and the thickness variations are significantly drastic in the vicinity of the collision point. In fig.4(d), due to numerical resolution, there are two blurry shadows corresponding to the invisible area in fig.4(a), as these fringes must be captured at a very precise angle. Based on the numerical aperture and working distance of the lens in our system, when the angle of reflected light from LST deviates by 24.6 mrad, it cannot be collected. When the gradient of thickness variation exceeds 50 nm per micrometer and causes the sheet surface to tilt beyond the collection angle, the fringes can not be captured.

This phenomenon not only occurs near the collision point, if the surface of the sheet bends and no longer behaves like a mirror, the integrity of the interference fringes will be damaged. The unevenness of LST can occur due to various factors, and fig.4(e) shows a case caused by asymmetry of flow rate. The sheet is bent and ripples appear on the surface, the thickness gradient at some positions reaching hundreds of nm per micrometer. The asymmetry of the leftmost subgraph reaches 3%, gradually improving to the right until it is completely symmetrical. The asymmetry of the flow rate has such a significant impact on the flatness of LST, so we use two pumps to independently control the two jets, avoiding asymmetry and instability caused by three-way splitting. In fact, we find that different asymmetric factors can cause different bending modes of the liquid sheet, including non-uniformity of mixed solutions, misalignment collision of the jet, asymmetry of flow rate, uneven end face of capillary outlet and so on, which will reflect in the interference fringes. This feature allows real-time monitoring of the flatness of LST as the sheet is always in a changing state. This significantly contributes to the stability and controllability of laser ion acceleration.

In summary, we realized the reconstruction of the two-dimensional thickness distribution of LST through the interference fringes for the fist time, and the thickness of the flat area varies monotonically with a gradient less than 0.5 nm per micrometer. Based on the pattern of the fringes, diagnosis and feedback of stable operation was achieved, ensuring the flatness of LST.

https://doi.org/10.1017/hpl.2023.101 Published online by Cambridge University Press

Tilt Angle Measurement

In laser ion acceleration, ions typically emit perpendicular to the surface of the film. If the target normal is not precisely oriented towards the collimation entrance of the ion energy spectrometer, the measured energy spectra may not be accurate. Moreover, in applications where ions are collected and transported with magnets, the correct orientation of the targets is crucial for designed beam transportation. The tilt angles of solid film targets can be measured and adjusted mechanically, but this is not feasible for self-supporting LSTs. Our diagnostic system includes a module to measure the tilt angles of LSTs to ensure correct orientation.

As depicted in fig.5(a), a reference mirror first replaces the LST and reflects the probe light to CCD2 via a polarization beam splitter (PBS) cube. The image spot on CCD2 serves as the reference position. Thereafter, the reference mirror is switched to the LST. The change in the position of the spot can be used to calculate the change in the tilt angle based on the object-image relationship. In our system, the probe light is initially rotated to s-polarized by a half-wave plate. After passing through PBS, light reflected from the rear surface of PBS will not enter CCD2. The light reflected from LST is converted to p-polarized after passing through a quarter-wave plate twice. It will eventually enter CCD2. This compact design effectively eliminates the reflection from the PBS, resulting in a good signal to noise ratio for the measurement. The rightmost subgraph in fig.5(d) shows a typical reflection spot collected by CCD2. The tilt angle of the LST can be calculated by the offset of the center of the reflection spot with respect to the reference position.

The measurement accuracy can reach 0.2 mrad in our system, which is obtained from the object-image relationship: the magnification of our system is 0.21, and the distance between the object plane and LST is about 160 mm. The physical resolution of the CCD is 1.34 μm. Assuming that the reflected light spot can be detected by moving 5 pixels (in fact, using our algorithm to calculate the center of the light spot can achieve an accuracy of 2-3 pixels), the resolution on the image plane is 6.7 μm, which is converted to 31.9 μm on the object plane. The field angle for the liquid sheet is 0.2 mrad, which is sufficient for tilt angle diagnosis in laser ion acceleration.

Fig.5(b) shows an example measurement of the deviation of LST's tilt angle in 1 hour, the tilt angle of LST naturally jitters by several milliradians. If the tilt angle deviates significantly due to some reason, this diagnosis allows us to detect and recover it in time. The liquid sheet can be accurately regulated to point in the the

https://doi.org/10.1017/hpl.2023.101 Published online by Cambridge University Press

expected direction in two dimensions by adjusting the flow rate of the two pumps and the misalignment of collision.

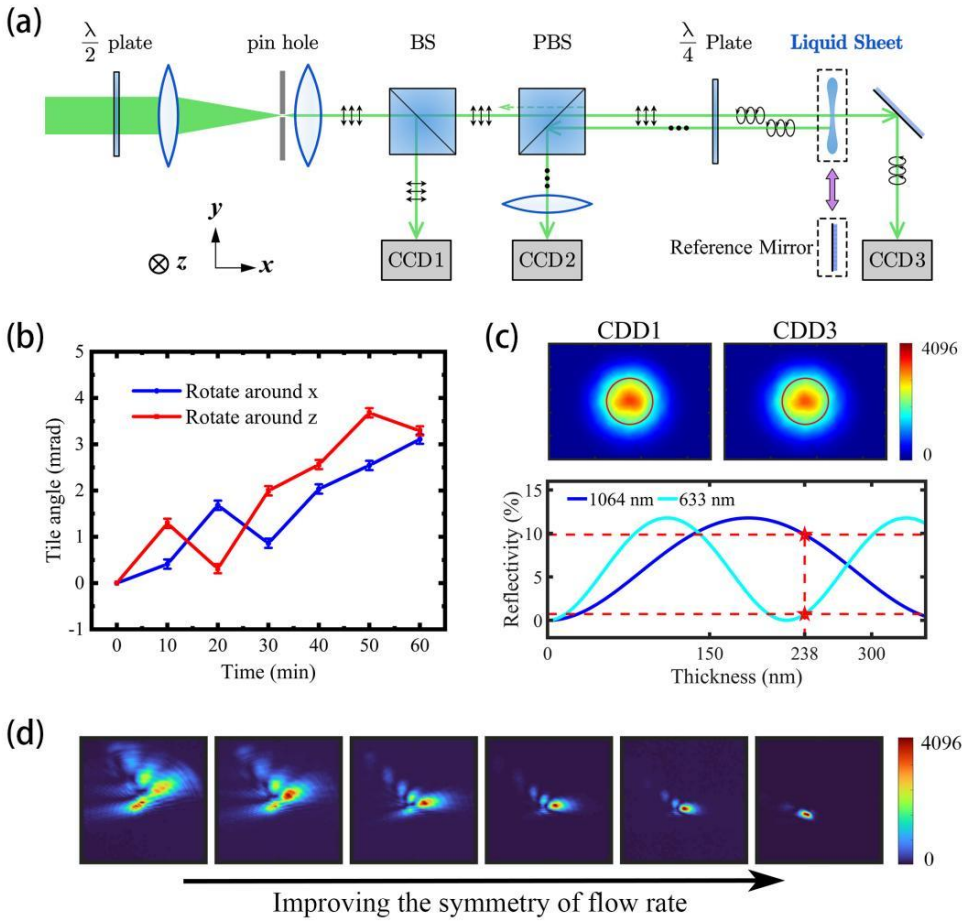

Fig.5 (a)Schematic diagram of tilt angle measurement, (b)The tilt angle change of LST within 1 hour (the definition of the coordinate axis can be found in fig.1(b) and fig.5(a)), (c)The intensity integral of CCD1 and CCD3 for calculating absolute reflectivity of LST, (d)The change of spot collected by CCD2 with the improvement of flow symmetry.

CCD3 behind LST is used to image the sheet and the light spot on the sheet(the same CCD in fig.2(a)). This helps identify the exact location where the tilt angle of LST is measured, as the sheet may have different tilt angles at different positions due to distortion. CCD3 and CCD1 also form a spectroscopic path for measuring the thicknesses of LSTs thinner than 300 nm. Two co-propagating lasers with different wavelengths are irradiated on CCD1 and CCD3, as shown in fig.5(c), then the reflectivity of the film is calculated by measuring the integrated light intensity of CCD1 and CCD3 simultaneously to eliminate the impact of light source jitter. A pure and smooth film like a liquid sheet can exhibit minimal surface scattering, thus its absolute reflectance is measured. The theoretical reflectivity, calculated from equation(1), is illustrated by the two sine curves in fig.5(c), while the red pentagram

https://doi.org/10.1017/hpl.2023.101 Published online by Cambridge University Press

denotes the reflectivity measured at two distinct wavelengths. Analysis of this data suggests a film thickness of 238 nm, which is consistent with the results presented in the "Thickness Measurement" section at 240 nm. The resolution of this method for s-polarized light can be represented by the following equation:

$$(\frac{\partial R}{\partial h})^{-1} = \frac{\lambda\left\{4\cos^2\theta\left[n^2(\lambda)-\sin^2\theta\right]+\left[n^2(\lambda)-1\right]^2\sin^2\left[2\pi h\sqrt{n^2(\lambda)-\sin^2\theta}/\lambda\right]\right\}^2}{8\pi\cos^2\theta\left[n^2(\lambda)-\sin^2\theta\right]^{\frac{3}{2}}\left[n^2(\lambda)-1\right]^2\sin\left[4\pi h\sqrt{n^2(\lambda)-\sin^2\theta}/\lambda\right]} \quad (3)$$

Assuming that $n=1.43,\ \theta=0,\ \lambda=633nm$, when the measured thickness is 238 nm, the result calculated from equation(3) is $\Delta h/\Delta R \approx 1175\text{nm}$. If $\Delta R = 0.1\%$ (this has been validated), then $\Delta h = 1.175\text{nm}$. This means that the thickness measurement result with error is 238 ±1.2 nm.

Furthermore, CCD2 not only diagnoses the tilt angle of the sheet, but also provides more information about the flatness of the sheet near the measurement point. The distortion of the film due to the imbalance of the two colliding liquid flows would result in an aberrant image of the spot, similar to that caused by a non-flat mirror. By adjusting the jets, an ideal reflection spot can be achieved as illustrated in fig.5(d). As the symmetry of the flow rate improves, the center of the reflected spot gradually shifts, indicating that the tilt angle of LST changes. Compared to fig.4(e), which has a 3% asymmetry of flow rate, the method in fig.5(d) provides a preciser but more localized characterization of flatness with only 1% asymmetry of flow rate.

In summary, we have built an integrated module to measure the tilt angle of LST with an accuracy of ±0.1 mrad. It also provides a quick and high-precision measurement of LST's thickness and local flatness.

Position Measurement

The results of laser ion acceleration closely relates to the relative positions of the laser focal spot and the target. Unlike solid films whose positions can be identified by defects or pollutants[26], a liquid sheet is transparent and flawless, thereby we utilized a confocal displacement detector (Micro-Epsilon, confocalDT 2421) to measure the position of LST.

The detector is arranged in the normal direction of LST and can be moved by a linear stage, as shown in fig.6(a). We first used a reference object to define this plane, and then used a CCD with very small depth of field (a few μm) to image it clearly. Main laser was focused by OAP to this plane as well. The confocal detector is then

https://doi.org/10.1017/hpl.2023.101 Published online by Cambridge University Press

used to measure the position of LST and make it coincide with the focusing plane.

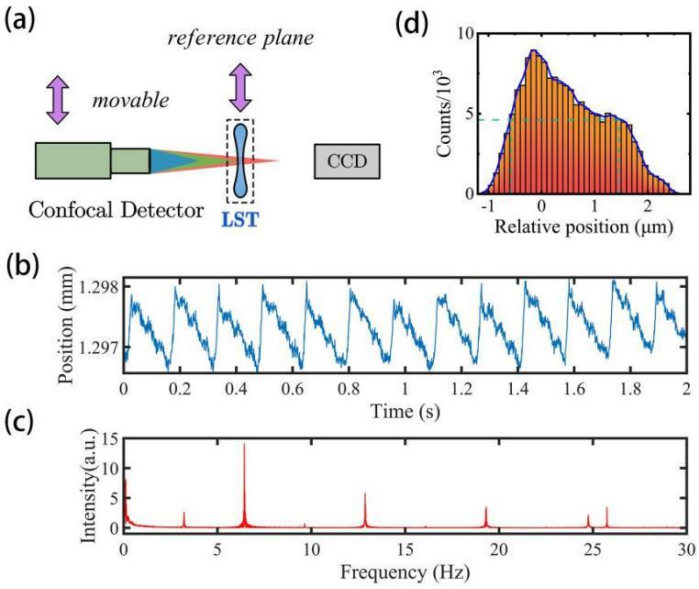

Fig.6 (a)Schematic diagram of position measurement, (b)Time domain of LST's position (distance to the confocal detector), (c)Frequency domain of LST's vibration in (b), (d)Histogram of LST's relative position within 10 minutes.

Fig.6(b) shows the periodic vibration of LSTs position, which is detrimental to laser ion acceleration. Therefore, we analyzed it in the frequency domain, as shown in Fig.6(c), revealing that vibration can be attributed to specific frequencies. We found that 6Hz and its multiples are derived from pump plunger motion, while the rest include capillary vibration, platform inherent vibration, and so on. Fig.6(d) is a histogram of the position (or amplitude of vibration) of a LST within 10 minutes after optimization. Its FWHM is approximately 2 μm, which is smaller than the Rayleigh length of the focused laser. Some relevant discussions on how to suppress the LSTs' jitter can be found in our publication[9].

Conclusions and Perspectives

In this work, we present a comprehensive diagnostic system for real-time and in-situ characterization of liquid sheet targets in a vacuum chamber. Reflectance spectroscopy and interference fringes are employed to precisely measure LST thickness over the entire area, while their tilt angles and spatial positions are also measured simultaneously. We identified crucial parameters that impact the thickness of LSTs and investigated how flow asymmetry affects their flatness and tilt angles. This information enables precise and closed-loop control of LSTs, which is crucial for

https://doi.org/10.1017/hpl.2023.101 Published online by Cambridge University Press

laser-driven ion acceleration and other applications[27]-[32]. Furthermore, our system and methods are also suitable for real-time, high-precision diagnosis of transparent solid film targets.

References

[1] Higginson A, Gray R J, King M, et al. Near-100 MeV protons via a laser-driven transparency-enhanced hybrid acceleration scheme[J]. Nature communications, 2018, 9(1): 724.

[2] Wang P, Gong Z, Lee S G, et al. Super-heavy ions acceleration driven by ultrashort laser pulses at ultrahigh intensity[J]. Physical Review X, 2021, 11(2): 021049.

[3] Daido H, Nishiuchi M, Pirozhkov A S. Review of laser-driven ion sources and their applications[J]. Reports on progress in physics, 2012, 75(5): 056401.

[4] Vozenin M-C, Bourhis J, Durante M. Towards clinical translation of flash radiotherapy. Nat Rev Clin Oncol (2022) 19(12):791 – 803. doi:10.1038/s41571-022-00697-z

[5] George K M, Morrison J T, Feister S, et al. High-repetition-rate (kHz) targets and optics from liquid microjets for high-intensity laser – plasma interactions[J]. High Power Laser Science and Engineering, 2019, 7.

[6] Morrison J T, Feister S, Frische K D, et al. MeV proton acceleration at kHz repetition rate from ultra-intense laser liquid interaction[J]. New Journal of Physics, 2018, 20(2): 022001.

[7] Valdes P P, de Luis D, Hernandez J, et al. Implementation of a thin, flat water target capable of high-repetition-rate MeV-range proton acceleration in a high-power laser at the CLPU[J]. Plasma Physics and Controlled Fusion, 2022.

[8] Treffert F, Curry C B, Chou H G J, et al. High-repetition-rate, multi-MeV deuteron acceleration from converging heavy water microjets at laser intensities of 1021 W/cm2[J]. Applied Physics Letters, 2022, 121(7): 074104.

[9] Cao Z, Peng Z, Shou Y, et al. Vibration and jitter of free-flowing thin liquid sheets as target for high-repetition-rate laser-ion acceleration[J]. Frontiers in Physics, 2023, 11: 231.

[10] Ma WenJun, Liu Zhipeng, Wang Pengjie, et al. 2021 Acta Physica Sinica **70** 15.

[11] Li R, Ashgriz N. Characteristics of liquid sheets formed by two impinging jets[J]. Physics of fluids, 2006, 18(8): 087104.

[12] Born M, Wolf E. Principles of optics: electromagnetic theory of propagation,

https://doi.org/10.1017/hpl.2023.101 Published online by Cambridge University Press

interference and diffraction of light[M]. Elsevier, 2013.

[13] Watanabe A, Saito H, Ishida Y, et al. A new nozzle producing ultrathin liquid sheets for femtosecond pulse dye lasers[J]. Optics Communications, 1989, 71(5): 301-304.

[14] Panao M R O, Delgado J M D. Effect of pre-impingement length and misalignment in the hydrodynamics of multijet impingement atomization[J]. Physics of Fluids, 2013, 25(1): 012105.

[15] Kashanj S, Kebriaee A. The effects of different jet velocities and axial misalignment on the liquid sheet of two colliding jets[J]. Chemical Engineering Science, 2019, 206: 235-248.

[16] Galinis G, Strucka J, Barnard J C T, et al. Micrometer-thickness liquid sheet jets flowing in vacuum[J]. Review of Scientific Instruments, 2017, 88(8): 083117.

[17] Koralek J D, Kim J B, Brůža P, et al. Generation and characterization of ultrathin free-flowing liquid sheets[J]. Nature communications, 2018, 9(1): 1353.

[18] Menzi S, Knopp G, Al Haddad A, et al. Generation and simple characterization of flat, liquid jets[J]. Review of Scientific Instruments, 2020, 91(10): 105109.

[19] Hoffman D J, Van Driel T B, Kroll T, et al. Microfluidic liquid sheets as large-area targets for high repetition XFELs[J]. Frontiers in molecular biosciences, 2022, 9: 1048932.

[20] Crissman C J, Mo M, Chen Z, et al. Sub-micron thick liquid sheets produced by isotropically etched glass nozzles[J]. Lab on a Chip, 2022, 22(7): 1365-1373.

[21] Barnard J C T, Lee J P, Alexander O, et al. Delivery of stable ultra-thin liquid sheets in vacuum for biochemical spectroscopy[J]. Frontiers in Molecular Biosciences, 2022, 9: 1044610.

[22] Goldstein R M, Zebker H A, Werner C L. Satellite radar interferometry: Two-dimensional phase unwrapping[J]. Radio science, 1988, 23(4): 713-720.

[23] Abdul-Rahman H S, Gdeisat M A, Burton D R, et al. Fast and robust three-dimensional best path phase unwrapping algorithm[J]. Applied optics, 2007, 46(26): 6623-6635.

[24] Chen M, Pukhov A, Yu T, et al. Enhanced collimated GeV monoenergetic ion acceleration from a shaped foil target irradiated by a circularly polarized laser pulse[J]. Physical review letters, 2009, 103(2): 024801.

[25] Hasson D, Peck R E. Thickness distribution in a sheet formed by impinging jets[J]. AIChE Journal, 1964, 10(5): 752-754.

[26] Shou Y, Wang D, Wang P, et al. Automated positioning of transparent targets

https://doi.org/10.1017/hpl.2023.101 Published online by Cambridge University Press

using defocusing method in a laser proton accelerator[J]. Nuclear Instruments and Methods in Physics Research Section A: Accelerators, Spectrometers, Detectors and Associated Equipment, 2019, 927: 236-239.

[27] Loh Z H, Doumy G, Arnold C, et al. Observation of the fastest chemical processes in the radiolysis of water[J]. Science, 2020, 367(6474): 179-182.

[28] Yang J, Dettori R, Nunes J P F, et al. Direct observation of ultrafast hydrogen bond strengthening in liquid water[J]. Nature, 2021, 596(7873): 531-535.

[29] Lin M F, Singh N, Liang S, et al. Imaging the short-lived hydroxyl-hydronium pair in ionized liquid water[J]. Science, 2021, 374(6563): 92-95.

[30] Barnard J C T, Lee J P, Alexander O, et al. Delivery of stable ultra-thin liquid sheets in vacuum for biochemical spectroscopy[J]. Frontiers in Molecular Biosciences, 2022: 1265.

[31] Yiwen E, Zhang L, Tsypkin A, et al. Progress, challenges, and opportunities of terahertz emission from liquids[J]. JOSA B, 2022, 39(3): A43-A51.

[32] Xia C L, Li Z L, Liu J Q, et al. Role of charge-resonance states in liquid high-order harmonic generation[J]. Physical Review A, 2022, 105(1): 013115.

https://doi.org/10.1017/hpl.2023.101 Published online by Cambridge University Press